



# Chemical bonding interface in Bi<sub>2</sub>Sn<sub>2</sub>O<sub>7</sub>/BiOBr S-scheme heterojunction triggering efficient N<sub>2</sub> photofixation

Yi Zhang<sup>a</sup>, Jun Di<sup>b,\*</sup>, Xingwang Zhu<sup>c</sup>, Mengxia Ji<sup>a</sup>, Chao Chen<sup>d</sup>, Yanan Liu<sup>a</sup>, Lina Li<sup>a</sup>,  
Tiange Wei<sup>a</sup>, Huaming Li<sup>a</sup>, Jiexiang Xia<sup>a,\*</sup>

<sup>a</sup> School of Chemistry and Chemical Engineering, Institute for Energy Research, School of the Environment and Safety Engineering, Jiangsu University, 301 Xuefu Road, Zhenjiang 212013, PR China

<sup>b</sup> School of Chemistry and Chemical Engineering, National Special Superfine Powder Engineering Research Center, Nanjing University of Science and Technology, Nanjing 210094, PR China

<sup>c</sup> College of Environmental Science and Engineering, Yangzhou University, Yangzhou 225009, PR China

<sup>d</sup> School of Materials Science & Engineering, Nanyang Technological University, Singapore 639798, Singapore

## ARTICLE INFO

### Keywords:

Chemical bonding interfaces  
S-scheme heterojunction  
Bi<sub>2</sub>Sn<sub>2</sub>O<sub>7</sub>  
BiOBr  
Photocatalytic nitrogen fixation

## ABSTRACT

Rapid recombination of interfacial charges is considered to be the main obstacle limiting N<sub>2</sub> photofixation. It is urgent but challenging to develop a precise and stable strategy to steer charge transfer. Herein, oxygen-vacancy-rich Bi<sub>2</sub>Sn<sub>2</sub>O<sub>7</sub> (BSO) are designed to be mounted on ultrathin BiOBr (BOB) with Bi-O vacancy pairs to construct the chemical bonding interface. The Bi and O atoms exposed by defects form the new Bi-O bonds to strengthen the built-in electric field, thus constructing the Bi<sub>2</sub>Sn<sub>2</sub>O<sub>7</sub>/BiOBr (BSOB) S-scheme heterojunction. During irradiation, electrons in CB of BOB rapidly recombine with holes in VB of BSO, and the electrons enriched in CB of BSO endow the strong reduction power for BSOB to trigger efficient photocatalytic nitrogen reduction. The ammonia yield of BSOB can reach 459.04 μmol g<sup>-1</sup> h<sup>-1</sup> in pure water. This work provides atomic-scale insights for the construction of efficient S-scheme heterojunction photocatalyst based on chemical bonding interface.

## 1. Introduction

Ammonia is an important chemical raw resource for agricultural production and chemical synthesis [1–3]. Nowadays, the ammonia synthesis reaction is mainly realized by Haber-Bosch process under high temperature and pressure environment, because of the high stability of N≡N bonds [4,5]. To make the nitrogen fixation reaction proceed under milder and energy-saving conditions, photocatalysis is expected as an alternative means [6,7]. However, the catalytic reaction involves multiple electron and proton transfer processes, thus making the design of catalyst challenging [8–11].

Semiconductor quantum dots and nanoparticles show great preponderance in light harvesting and exciton generation due to quantum effects [12]. The surface of these materials is rich in unsaturated functional groups and edge sites [13], which also provides a basis for the rational design of photocatalytic N<sub>2</sub> reduction. Unfortunately, although most of them can be efficiently excited due to their narrow band gaps, they usually annihilate rapidly because of the thermalization of photoelectrons [14]. In order to enforce quantum confinement, wide-bandgap

materials are considered as the ideal platform for hosting excited electrons and optimizing the migration process [15]. Researchers have achieved improved photocatalytic performance by constructing heterojunction materials, such as SnO<sub>2</sub>-x/BiOI (PN junction) [16], vanadate QDs/g-C<sub>3</sub>N<sub>4</sub> (type-II heterojunctions) [17], HJ-C<sub>3</sub>N<sub>4</sub> (type-I heterojunctions) [18]. Notably, although these types of heterojunction structures can achieve spatial separation of photogenerated carriers, the overall redox ability of the material is partly weakened. The construction of Z- and S-scheme heterojunctions provides the solutions. Guo et al. designed In<sub>2</sub>O<sub>3</sub>-ZnSe-Mo Z-scheme nanosheets to achieve a significant improvement in the photocatalytic hydrogen production [19]. Yu et al. constructed a new type TiO<sub>2</sub>/CsPbBr<sub>3</sub> S-scheme heterojunction to promote photocatalytic CO<sub>2</sub> reduction [20]. By recombining the holes of the reduction semiconductor with the electrons of the oxidation semiconductor, the strong reduction ability of the photocatalyst could be preserved. Therefore, upon QDs or nanoparticles anchoring in the semiconductor support, it is desirable to realize the rapid consumption of the carrier's photogenerated electron to the hole, so as to promote more electrons with high reduction capacity for photocatalytic N<sub>2</sub>

\* Corresponding authors.

E-mail addresses: [dijun@njust.edu.cn](mailto:dijun@njust.edu.cn) (J. Di), [xjx@ujss.edu.cn](mailto:xjx@ujss.edu.cn) (J. Xia).

<https://doi.org/10.1016/j.apcatb.2022.122148>

Received 27 August 2022; Received in revised form 21 October 2022; Accepted 6 November 2022

Available online 7 November 2022

0926-3373/© 2022 Elsevier B.V. All rights reserved.

fixation.

However, most heterojunction materials suffer from less contact and unstable surface states, making it difficult to form a strongly coupled interface for effective separation of charges [21,22]. Therefore, the precise control of the interface is urgently required. An effective strategy is the construction of defect-induced chemical bonds [23]. The surface unsaturated coordinating atoms and the region of delocalized local electrons caused by defects have higher surface free energy and affinity, which can serve as the connecting sites. On the basis of this atomic-level interface, the rigid construction of chemical bonds will endow materials unique property enhancements, such as enhancing the structural stability of the heterojunction interface, establishing fast electron diffusion paths and improving interfacial charge transport [24]. Most advanced reports focus on the effect of chemical bonds on charge transfer, but ignore the effect of interfacial effects as well as the modulation process of electronic structure and bandgap in compounds.

Herein, oxygen-vacancy-rich  $\text{Bi}_2\text{Sn}_2\text{O}_7$  nanoparticles (BSO) and ultrathin BiOBr (BOB) with Bi-O vacancy pairs are selected as research models. Through the defect-inducing strategy, the chemical bonding interface assembled by Bi-O bond in  $\text{Bi}_2\text{Sn}_2\text{O}_7/\text{BiOBr}$  (BSOB) is formed to realize the construction of S-scheme heterojunction, that not only realizes the rigid connection of the material interface, but also acts as a fast electron transfer path. When illuminated, electrons in the conduction band of BOB rapidly recombine with holes in the valence band of BSO due to interfacial electrostatic interactions. Ultimately, electrons enriched in the conduction band of BSO endow the strong reduction power for BSOB to trigger efficient photocatalytic nitrogen fixation. This work provides atomic-scale insights for the construction of efficient S-scheme heterojunction photocatalyst based on chemical bonding interface.

## 2. Experimental

### 2.1. Synthesis of BiOBr ultrathin nanosheets (BOB)

0.5 mmol of  $\text{Bi}(\text{NO}_3)_3 \cdot 5\text{H}_2\text{O}$  and 0.2 g of polyvinylpyrrolidone (PVP) were dissolved in 15 mL of mannitol (0.1 M), denoted as solution A. 0.5 mmol of NaBr was dissolved in 3 mL of deionized water, and denoted as solution B. The mixture was transferred to a 25 mL Teflon-lined autoclave and heated under 160 °C for 3 h. The reacted solution was centrifuged through high-speed centrifuge. The precipitate was collected and washed for 3 times each with deionized water and ethanol. The processed samples were placed in a vacuum drying oven until drying.

### 2.2. Synthesis of $\text{Bi}_2\text{Sn}_2\text{O}_7$ nanoparticles (BSO)

1 mmol  $\text{Na}_2\text{SnO}_4 \cdot 4\text{H}_2\text{O}$  was dissolved in 5 mL of mannitol as solution A. 1 mmol of  $\text{Bi}(\text{NO}_3)_3 \cdot 5\text{H}_2\text{O}$  and 0.3 g of polyvinylpyrrolidone (PVP) were dispersed in 15 mL mannitol (0.1 M) and marked as solution B. Then, solution A was slowly dropped into solution B under vigorous stirring. Subsequently, the pH of the mixture was adjusted to 12 with NaOH (2 M) and stirred for 30 min. Finally, it was transferred to a 25 mL Teflon-lined autoclave and heated under 200 °C for 24 h. The reacted solution was centrifuged through high-speed centrifuge. The precipitate was collected and washed for 3 times each with deionized water and ethanol. The processed samples were placed in a vacuum drying oven until drying.

### 2.3. Synthesis of $\text{Bi}_2\text{Sn}_2\text{O}_7/\text{BiOBr}$ (BSOB)

1 mmol of BOB and 2 mmol of BSO were uniformly dispersed in 20 mL of ethanol. The mixture was then placed in an agate mortar. The slurry was continuously ground under mercury lamp irradiation until dry. The powder was collected and washed for 3 times each with deionized water and ethanol. The processed samples were placed in a

vacuum drying oven until drying.

### 2.4. Photocatalytic nitrogen fixation experiment

Under standard atmospheric pressure, a 100 mL external circulating water quartz bottle was used as the reaction vessel to keep 25 °C. 50 mg of the sample was dispersed in 100 mL of deionized water. Then, the solution was purged with  $\text{N}_2$  ( $\geq 99.999\%$ ) and bubbled for 30 min under dark. A 300 W Xenon lamp was used as the light source, and a certain amount of solution was extracted from the reaction flask every 20 min for subsequent nitrogen fixation performance analysis.

Ammonia production was further analyzed by Nessler's reagent method. During the reaction, a certain amount of supernatant was centrifuged and filtered through a 0.22  $\mu\text{m}$  membrane filter. The solution was diluted with water to a specific ratio and transferred to a 5 mL colorimetric tube, then potassium and sodium tartrate solution and Nessler reagent were added. After mixing, let stand for a period of time to produce color reaction and test by UV-Vis spectrophotometer (UV-2450, Shimadzu) at  $\lambda = 420$  nm. Finally, the concentration of bound nitrogen was calculated through the absorbance of the sample.

### 2.5. In situ Fourier transform infrared experiment

The sample was placed in the in-situ cell and keep the surface flat. After the reaction system was loaded, argon was introduced and the temperature was programmed to 120 °C for 0.5 h to remove impurities adsorbed on the surface, at a rate of 5 °C/min. The MCT detector was then invoked to acquire the signal, with the sample under argon as the background. Moist  $\text{N}_2$  gas was bubbled in and the dark adsorption data of the samples were recorded. After reaching the adsorption equilibrium, turn on the high uniformity integrated Xenon light source (Beijing Perfectlight, PLS-FX300HU) and record its corresponding spectrum.

## 3. Results and discussion

### 3.1. Composition and morphology of BSOB

Oxygen-vacancy-rich BSO nanoparticles and ultrathin BOB with Bi-O vacancy pairs exposed the mutual Bi, O atoms on surface to enhance interfacial adaptation, thus enabling the synthesis of BSOB. X-ray diffraction (XRD) analysis was carried out to detect compounding of materials. In Fig. S1, peaks at 25.2°, 31.8°, 46.2° and 57.2° are corresponded to (1 0 1), (1 0 2), (2 0 0) and (2 1 2) planes of BiOBr (JCPDS No. 73-2061), respectively. Meanwhile, peaks at 28.9°, 33.4°, 48.0° and 57.9° are belong to (0 2 4), (0 2 8), (2 2 0) and (-2 -2 12) planes of  $\text{Bi}_2\text{Sn}_2\text{O}_7$  (JCPDS No. 96-432-6954). The corresponding characteristic peaks of BSOB indicate the successful construction of the composite. Atomic force microscope (Fig. S2) and TEM (Fig. S3) were used to reveal the thickness and morphology of the materials. It can be observed that BOB is an ultrathin nanosheet with an atomic layer thickness of about 1 nm, and BSO shows nanoparticle structure with size less than 10 nm. When these two materials are combined, BSO can be freely dispersed in the lamellar structure of BOB, effectively avoiding agglomeration. Aberration-corrected high-angle annular dark-field scanning transmission electron microscopy (HAADF-STEM) was applied to further reveal the microstructure at atomic scale. Two lattice stripes of 0.277 nm at an angle of 90° can be observed in BOB (Fig. 1a), which are corresponded to the (1 1 0) crystal plane [25], indicating the exposure of (0 0 1) plane. The point defects associated with Bi vacancies cause the structural collapses of continuous atomic sizes, which show as partial dark spots in the atomic arrangement [26]. In Fig. 1b, BSO exhibits a quantum dot structure with a size of about 5 nm, and the lattice spacing of 0.268 nm is attributed to the (0 2 8) crystal plane. After combination (Fig. 1c-e), there is an obvious interface between BSO and BOB. The lattice of 0.309 nm on the upper layer corresponds to the (0 2 4) plane of BSO [27], meanwhile some Bi associated vacancies in BOB can still be

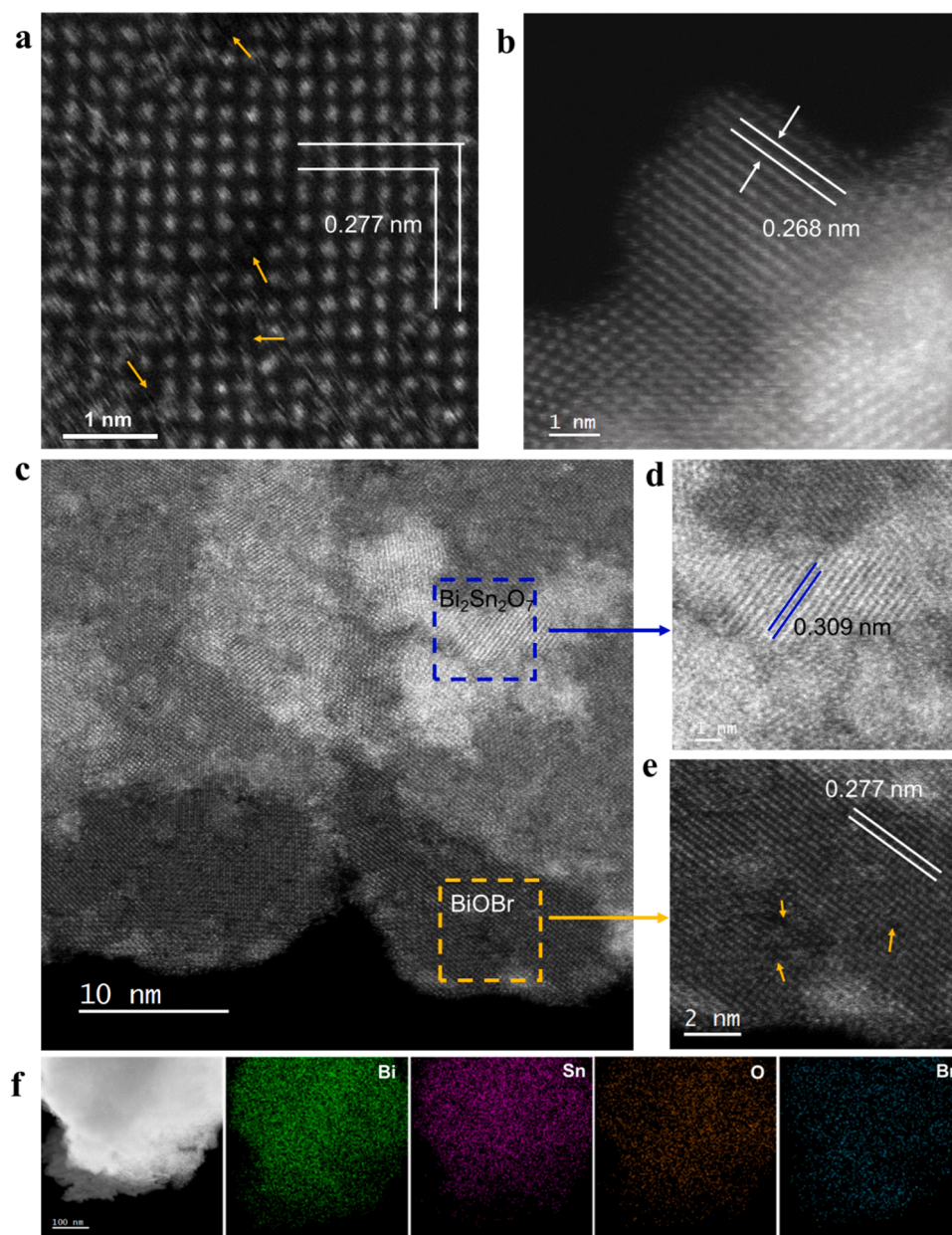


**Fig. 1.** The atomic resolution HAADF-STEM images of (a) BOB, (b) BSO, (c-e) BSOB; (f) STEM-EDS mapping images of BSOB.

observed in the bottom layer. Their shared Bi, O atoms create conditions for lattice matching, and the copious surface dangling bonds induced by defects would facilitate the formation of covalent bonds, so as to construct the strong interfacial connection. As shown in Fig. 1f and S4, HAADF-STEM-EDS elemental mapping images manifest the uniform distribution of Bi, Sn, O, Br atoms in BSOB composite material.

### 3.2. Chemical bonding interface in BSOB

Furthermore, the interaction between BOB and BSO in BSOB was deeply explored. Zeta potential test (Fig. 2a) shows that the surfaces of BOB and BSO are oppositely charged, and BSOB are presumed to be constructed by electrostatic self-assembly [28]. Compared with BSO, the potential value of BSOB is larger, indicating that it is more stable in the aqueous environment. The interaction of BSO with BOB in BSOB was subsequently investigated. As shown in Fig. S5, the Raman peaks associated with O'-Bi-O' bending ( $F_{1u}$ ) in BSOB exhibit a weakened intensity and shift in peak position, indicating that the strong interfacial contact

between BOB and BSO affects the structural stress of BSOB [29]. Then, the effects of changes in the state of related elements were further investigated by XPS (Fig. 2b, c). Compared with BOB and BSO, the Bi 4f peak of BSOB shifts from 164.2 eV to high binding energy, which is related to the loss of electrons from Bi atoms after the formation of effective interfacial contact. The peaks located at about 529.8, 531.7, 533.3 eV can be indexed to lattice oxygen, the oxygen atoms near the oxygen vacancies and surface hydroxyl, respectively [30]. The increased area of the proportion and the shifting to lower binding energy direction of the middle peak in BSOB indicate that more dangling oxygen atoms are generated near the vacancy and partially coordinated. EPR (Fig. 2d) provides information on unpaired electrons. BSOB shows the strongest symmetric EPR signal at  $g = 2.001$ , indicating that the composite possesses more spintronics. The changes of chemical bonds on the surface of the material were explored by infrared diffuse reflectance spectroscopy (Fig. 2e and S6). Different from the peaks at  $468\text{ cm}^{-1}$  for BOB and BSO, BSOB generates a new peak at  $456\text{ cm}^{-1}$ , which is attributed to the vibration of Bi-O [31], demonstrating the creation of new Bi-O bonds



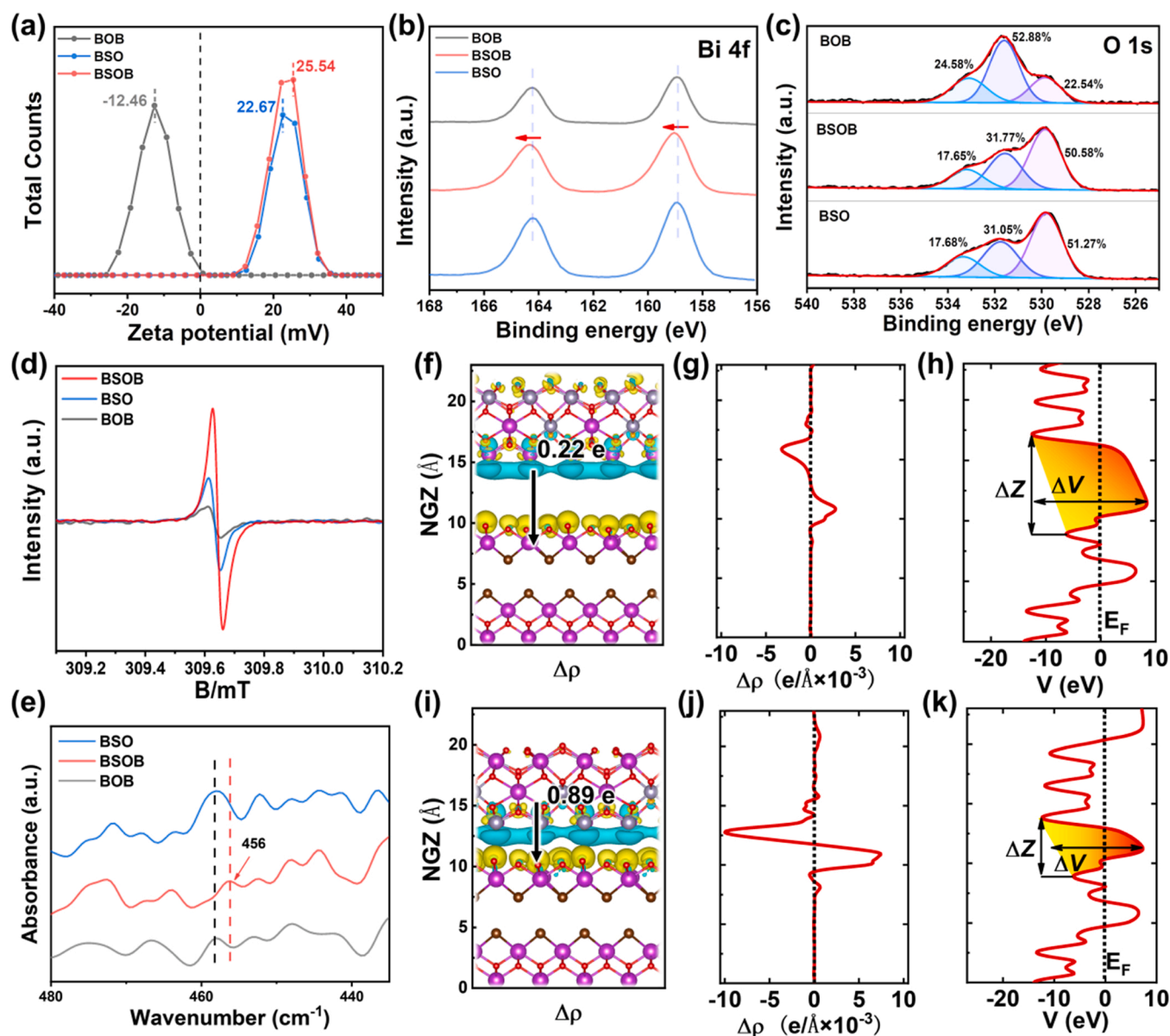


Fig. 2. (a) Zeta potential of the samples; (b) Bi 4f and (c) O 1s XPS spectra; (d) EPR spectra; (e) Infrared diffuse reflectance spectrum of the samples; Charge density difference for (f) physically mixing model and (i) chemical bonding model; (g), (j)  $\langle \Delta\rho \rangle$  averaged through the xy plane of the layers corresponding to different locations along the z axis; (h), (k) Electrostatic potential  $\langle V \rangle$  averaged through the xy plane of the layers corresponding to different locations along z axis.

between the interfaces.

The work functions are measured by ultraviolet photoelectron spectrometer (UPS) to investigate the electron transfer within the heterostructure. As shown in Fig. S7, the work functions of BOB and BSO are 7.42 and 6.66 eV, respectively, indicating that BSO has a higher Fermi level. When they come into contact, electrons will flow from BSO to BOB to enable the phases at the same Fermi level and create internal electric field between them. Theoretical calculations were used to simulate the electronic structural properties of the chemical bonding interface in BSOB, and a physical mixing model was constructed for comparison. In Fig. 2f, i, the color of yellow represents electron excess and blue represents electron deficiency. The  $\Delta\rho$  visualized by contour plots demonstrates that charge reforming region between chemical bonding interfaces in BSOB is more concentrated and stronger [32,33]. Then  $\Delta\rho$  was averaged in the planes with  $z = \text{const}$  (Fig. 2g, j), the chemical bonding interface model exhibits a significantly enlarged difference signal. Subsequently, the number of electron transfer in the model was quantified by Bader charge analysis. The results show that

0.89 e electrons are transferred from BSO to BOB through the chemical bonding interface, while the physical mixing model was only 0.22 e, which demonstrates that the chemical bonding interface has obvious advantages in the number of transferred electrons. Besides, considering that the charge transfer is limited by the potential energy barrier of the interface, the regional electrostatic potential of the heterojunction was further studied in Fig. 2h, k. Taking the potential hydrazine bottom as the benchmark, the physical hybrid model has the potential barriers of  $\Delta z \approx 8.25$  Å and  $\Delta V \approx 21.05$  eV. Also, there is still tunnel barriers of  $\Delta z \approx 6.01$  Å and  $\Delta V \approx 8.52$  eV for Fermi level electrons. While in chemical bonding interface, the barrier decreases to  $\Delta z \approx 4.97$  Å and  $\Delta V \approx 20.23$  eV, and the Fermi barrier reduced to  $\Delta z \approx 2.57$  Å and  $\Delta V \approx 7.48$  eV. Therefore, the energy barrier at the chemical bonding interface is lower and electrons can migrate more easily, indicating the chemical bonding interface favors to promote charge transfer across the heterojunction.

### 3.3. Photocatalytic performance of BSOB S-scheme heterojunction

Subsequently, the photocatalytic  $N_2$  reduction performance of the materials was validated. As shown in Fig. 3a and S8, 50 mg of catalyst is evenly dispersed in 100 mL of pure water without any sacrificial agent or photosensitizer. After irradiation for 60 min, BSOB exhibits the strongest photocatalytic nitrogen reduction performance to yield  $NH_3$  ( $459.04 \mu\text{mol g}^{-1} \text{h}^{-1}$ ), which is 1.4 times ( $326.12 \mu\text{mol g}^{-1} \text{h}^{-1}$ ) of BSO and 5.5 times ( $83.76 \mu\text{mol g}^{-1} \text{h}^{-1}$ ) of BOB. The ammonia yield of BSOB is highly competitive with many previously reported state-of-the-art

photocatalysts (Table S1) tested under similar conditions [34–44]. The values of ammonia yield of BSOB measured by indophenol blue method are approximated ( $436.20 \mu\text{mol g}^{-1} \text{h}^{-1}$ ). Moreover, the ammonia yield of BSOB was only  $3.62 \mu\text{mol g}^{-1} \text{h}^{-1}$  under Ar atmosphere, which is caused by the adsorbed  $N_2$  on the surface. Isotopic experiments (Fig. 3b) were further used to reveal the source of nitrogen, the corresponding triplet and doublet peaks in NMR spectrum are assigned to  $^{14}NH_4Cl$  and  $^{15}NH_4Cl$ , respectively, indicating that ammonium in solution as produced only by the reduction of  $N_2$  molecules exclusively. The typical sample exhibits stable photocatalytic properties and morphological

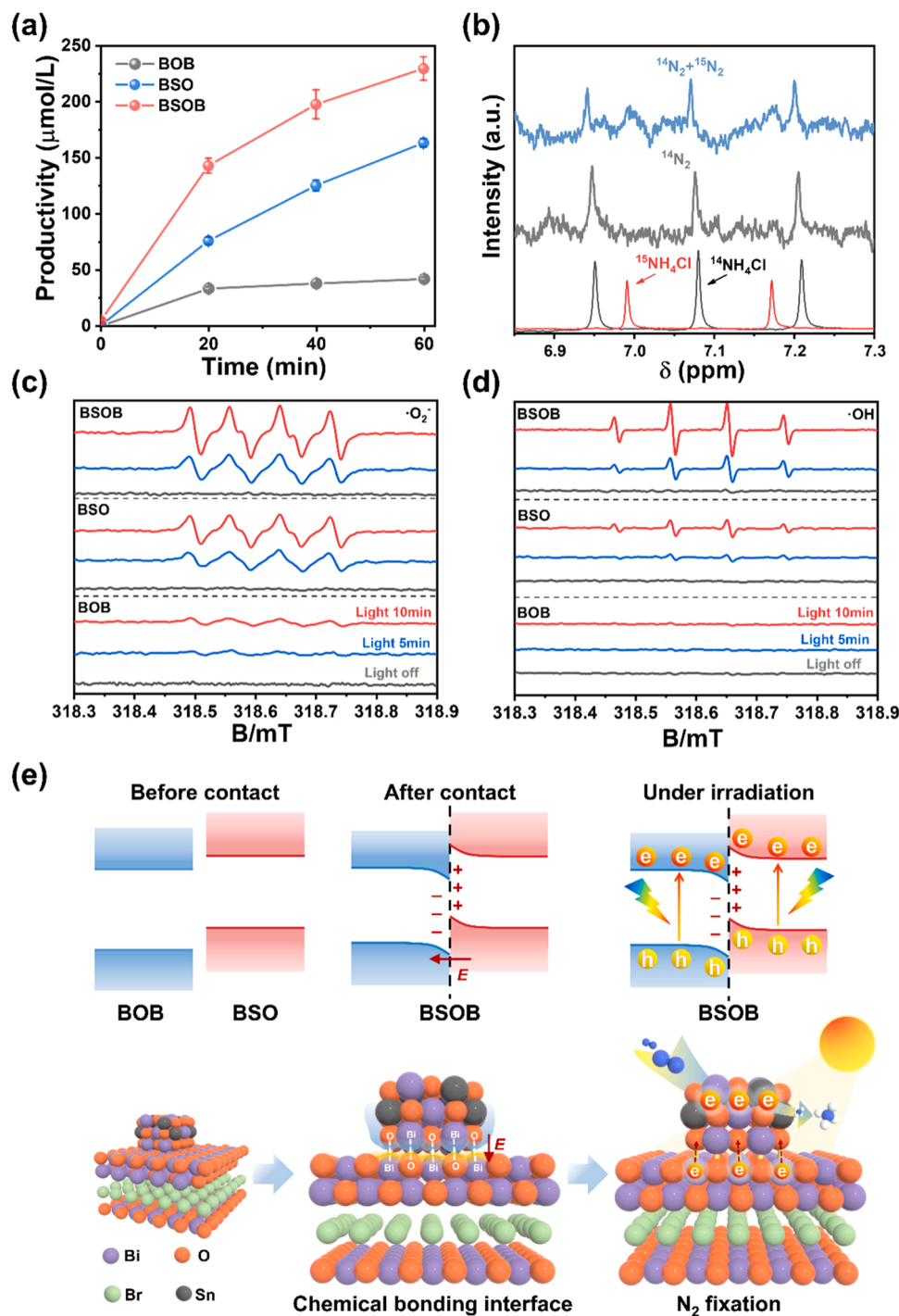


**Fig. 3.** (a) Quantitative determination of the generated ammonia; (b)  $^1\text{H}$  NMR (400 MHz) spectra of BSOB at different atmosphere; DMPO spin-trapping ESR spectra of as-prepared samples detected in (c) methanol and (d) aqueous dispersion; (e) The inferred electronic structure model and the mechanism of photocatalytic nitrogen fixation.

structures. Cycling experiments (Fig. S9) show that the activity of material can still maintain more than 88 % after 5 cycles. The samples after the reaction were collected, and the results show that the crystal structure of BSOB do not change significantly (Fig. S10 and S11), and the BSO are still well distributed on the BOB (Fig. S12). Furthermore, the solution after the reaction was measured (Fig. S13–15). The concentration of  $\text{N}_2\text{H}_4$  in the solution was quantified by Watt and Chrisp method, and the yield of BSOB is only  $0.23 \mu\text{mol g}^{-1} \text{h}^{-1}$ , showing a high electron selectivity to ammonia. In Fig. S14, the presence of  $\text{H}_2\text{O}_2$  was also detected in the solution, indicating that holes can be dissipated by generating such oxygen species. Based on the consideration of thermodynamic factors to explore the reasons for the performance improvement, the electronic structure optimization of the material was further studied. UV-vis diffuse reflectance spectra (Fig. S16) show the light absorption capacity of the materials. Then, the band gaps (Fig. S17) of BOB and BSO are calculated by Kubelka-Munk function transformation [45], which are 2.64 and 2 eV, respectively. The valence band (VB) values of materials could be obtained based on energy information of VB-XPS (Fig. S18). Specifically, the VB of BOB is calculated to be 1.65 eV and the corresponding conduction band (CB) is  $-0.99$  eV, while BSO are 0.8 and  $-1.2$  eV, respectively. As shown in Fig. S19, all samples have a positive slope and exhibit typical n-type semiconductor characteristics. The  $E_{\text{FB}}$  of BOB, BSO and BSOB are  $-0.67$ ,  $-0.75$  and  $-0.70$  eV vs Ag/AgCl electrode, respectively. Then, the  $E_{\text{FB}}$  can be calculated as  $-0.473$ ,  $-0.553$  and  $-0.503$  vs NHE. The electrochemical signal (Fig. S20) reveals the relative efficiency of electron transfer in samples. BOB exhibits lower photo-induced charge separation, leading to its weaker reduction ability. The light absorption ability of BSOB is weaker than that of BSO. Due to the rapid transfer of electrons through the chemical bonding interface, it retains most of the photogenerated electrons, showing the strongest current density. Also, from electrochemical impedance spectrum (EIS) (Fig. S21), BSOB has the smallest Nyquist radius, verifying that BSOB with chemical bonding interface has a small mass transfer resistance for electrons, which matches the theoretical calculation results [46].

Transient fluorescence (Fig. S22) was used to study the flow behavior of electrons in BSOB through this interface. The datas are fitted by second-order exponential equation.  $\tau_1$ ,  $\tau_2$  represent the non-radiative process in electron transfer and the radiative process related to recombination, respectively. Compared to BOB and BSO, the entire electron relaxation process of BSOB mainly contributes to  $\tau_1$  and lasts the longest, indicating an enhancement of most photoinduced electron transfer [47]. BSOB exhibits a longer  $\tau_2$  but the smallest proportion, suggesting that the chemical bonding interface increases the electronic lifetime of the complex and reduces the recombination. As results, the average fluorescence lifetimes of BOB, BSO and BSOB are 2.8215, 3.1628 and 2.7311 ns, respectively. The calculated electronic structure was verified by electron spin resonance (ESR) tests later (Fig. 3c, d). Six enhanced DMPO- $\text{O}_2^{\cdot-}$  and four DMPO- $\text{OH}$  characteristic peaks can be detected in BSOB. Notably, the VB of BSOB does not conform to the usual hydroxyl radical generating potential (2.38 eV vs NHE). Herein, the generation of  $\cdot\text{OH}$  is achieved through this pathway:  $2 \cdot\text{O}_2 + 2 \text{H}^+ \rightarrow 2 \cdot\text{OH} + \text{O}_2$ . Considering that BOB does not generate  $\cdot\text{OH}$  signal, the enhancement of peaks in BSOB are caused by the transfer of electrons from BOB to BSO, and the multi-relaxation electronic state endows the material with stronger reducing ability. The separation of photogenerated charges is verified by the residual TEMPO signal (Fig. S23). Compared with BOB and BSO, BSOB show the strongest quenching degree for both  $\text{e}^-$  and  $\text{h}^+$ , indicating that the S-scheme heterojunction structure with chemical bonding interface can retain a large number of effective electrons through the built-in electric field and fast electron migration channels. Furthermore, oxygen production experiments were applied to reveal the distribution of holes (Fig. S24). The oxygen production of BSO is 0, while the oxygen production capacity of BOB is still retained in BSOB, indicating that oxygen production mainly occurs in BOB and holes are not transferred to BSO. Based on the above research findings, the schematic

diagrams of possible electronic structures and the mechanism of photocatalytic nitrogen fixation are presented in Fig. 3e. The chemical bonding interface in BSOB is formed by defect-induced strategy, and BSO achieves tight interfacial contact with BOB due to Bi-O bond. In this S-scheme heterojunction, BOB is applied to capture the photogenerated holes of BSO, and BSO acts as the active site for  $\text{N}_2$  photofixation. Specifically, electrons in BSO diffuse to BOB spontaneously, forming the electron depletion layer in BSO and electron accumulation layer in BOB. Affected by this built-in electric field, the energy bands of BOB and BSO bend and form S-scheme heterojunction. During irradiation process, the electrons of BOB and BSO are excited to transition to the CB. The electrostatic interaction at the interface makes the electrons in the CB of BOB recombine with the holes in the VB of BSO through Bi-O bond, resulting the enrichment of electrons in BSO. Finally, the surface Bi and Sn atoms around O vacancies in BSO act as the main active sites to realize the activation and reduction process of  $\text{N}_2$  through copious photogenerated electrons. Therefore, the S-scheme heterojunction constructed by the chemical bonded interface achieves effective separation of photo-generated charges and retains the strong reducing ability of BSOB for photocatalytic nitrogen fixation.

### 3.4. Mechanism of $\text{N}_2$ photofixation

Kinetics as one of the factors affecting the reaction also deserves to be considered. The water contact angle test (Fig. 4a) was used to investigate the hydrophilic properties of materials. Taking a quick shot when the droplet falls on the surface for 0.4 s, and the included angle of the BSOB is the smallest, which is  $15.6^\circ$ . Therefore, the BSOB surface easily maintains a water-rich interfacial environment, which is beneficial for the formation of H protons involved in  $\text{N}_2$  to  $\text{NH}_3$  conversion. Electrochemical tests were performed by linear sweep voltammetry (LSV) to investigate the competition between nitrogen fixation and hydrogen precipitation reactions (Fig. S25). In Ar gas, HER reaction occurs at the electrode surface due to the chemical inertness of Ar. When  $\text{N}_2$  was bubbled in, the conduction potential shifted to a low potential, indicating that NRR has a relatively lower overpotential than HER, suggesting that the nitrogen fixation reaction is more likely to occur on the sample surface [48]. The increase in current density under light verified the rapid photocatalytic nitrogen fixation reaction. The  $\text{N}_2$  adsorption capacity of the samples was explored by  $\text{N}_2$  temperature programmed desorption ( $\text{N}_2$  TPD) (Fig. S26). The initial desorption temperature of BSOB is between BOB and BSO, and it shows a medium signal intensity, indicating that the photocatalytic performance improvement has less correlation with nitrogen adsorption. Further, the adsorption, activation and reaction processes of  $\text{N}_2$  were deeply investigated through In situ Fourier transform infrared spectroscopy (FTIR) (Fig. 4b, c). As for BSOB, the peak at  $1648 \text{ cm}^{-1}$  is enhanced in dark adsorbed state and dissipated after illumination, which is ascribed to adsorbed  $\text{N}_2$  and  $\text{H}_2\text{O}$ . The predominant overlapped adsorption band ranging from  $3000$  to  $3700 \text{ cm}^{-1}$  can be observed, where the band at  $3550$  and  $3425 \text{ cm}^{-1}$  are assigned to the  $\nu(\text{N-H})$  stretching mode and the  $\nu(\text{O-H})$  stretching mode of adsorbed water, respectively. Moreover, The band at  $1355 \text{ cm}^{-1}$  is assigned to  $\text{NH-NH}$ , which is an intermediate in the hydrogenation with  $\text{N}_2$  [49]. Peaks located at  $1712$ ,  $1557$  and  $1190 \text{ cm}^{-1}$  are attributed to the adsorbed  $\text{NH}_3$ , and the increased peaks at  $1416$  and  $2935 \text{ cm}^{-1}$  could readily be assigned to surface  $\text{NH}_4^+$  [50]. The entire evolution process is visualized by in situ MCT-SEIRAS FTIR spectra (Fig. 4d, e). With the sample under Ar gas as the background, each 0.2 s to record its surface state. The bright yellow signals that appeared after the introduction of  $\text{N}_2$  indicate the efficient adsorption of the gas on the surface. Under irradiation, the transient inverse signal enhancements in blue and red indicate the rapid dissipation of  $\text{N}_2$  and  $\text{H}_2\text{O}$  as raw stuff, and the generation of the reduction product  $\text{NH}_4$ , respectively. The orange signal at  $1250 \text{ cm}^{-1}$  is assigned to  $\tau(\text{N-N})$  mode [51], demonstrating the efficient transfer of electrons to the adsorbed  $\text{N}_2$  and the weakening of the  $\text{N}\equiv\text{N}$  bond.



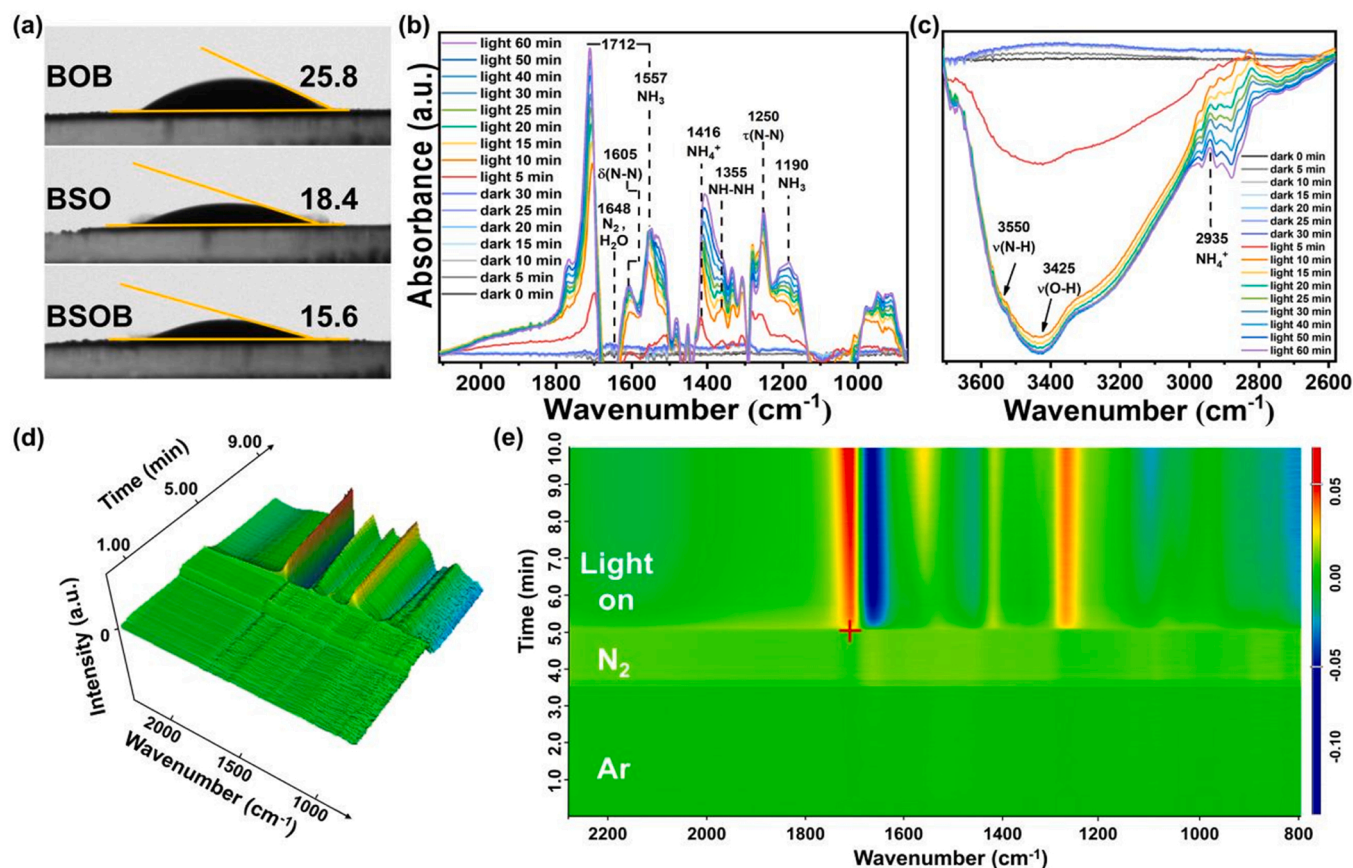


**Fig. 4.** (a) Static water contact-angle measurement; (b) and (c) In situ FTIR spectra for the  $N_2$  fixation process of BSOB; (d) 3D Time-resolved In situ MCT-SEIRAS FTIR spectra and (e) 2D contour color map corresponds to line plots with 0.2 s intervals for 10 min of BSOB.

### 3.5. DFT calculations of $N_2$ photofixation

Gibbs free energy calculations provide insight into the nature of the reaction of this process. In photocatalytic  $N_2$  reduction, the distal route is considered as a favorable mechanism for breaking  $N\equiv N$  bonds over Bi-based materials. As shown in Fig. 5 and S27–29, both BOB and BSO have large conversion energy of  $^*NNH_2$  to  $^*N$ , and the required uphill free energies are 2.22 and 0.86 eV, respectively, which limit the reaction. However, BSOB with the chemical bonding interfaces can spontaneously cleave the intermediate into individual adsorbed  $^*N$ . For BSO, there is a difficulty in overcoming the 2.00 eV energy barrier for the second formation and desorption of  $^*NH_3$ , while BSOB can reduce this process to 1.49 eV. For the entire  $N_2$  reduction process, the input energy requirement of BSOB is minimal, so it can be inferred that the construction of chemical bonding interface could trigger efficient  $N_2$  reduction. Since the protonation process is an important part for the conversion of  $NH_3$ , the adsorption of H atoms on the surface of the material was further analyzed. The larger value of  $\Delta G_H^*$  means that it is more difficult to convert the H intermediate to molecular hydrogen [52]. The  $\Delta G_H^*$  of BSOB is the smallest among them, which is favorable for the generation of  $H^*$ , thereby promoting the hydrogenation of  $N_2$  to generate  $NH_3$ . Compared with Pt (−0.09 eV), the  $\Delta G_H^*$  of BSO (−0.21 eV) and BSOB (−0.19 eV) is more negative, resulting in slow reaction kinetics. The strong adsorption of H protons on the surface of the material will hinder the occurrence of the competing reaction-HER, that creates conditions for the protonation process of the N intermediate in the nitrogen fixation reaction.

## 4. Conclusion

In summary, S-scheme heterojunction BSOB with chemical bonding

interface for efficient photocatalytic nitrogen fixation is designed. The newly formed Bi-O bonds act as the main connecting unit between the defective interfaces, which strengthen the interfacial coupling and work as fast electron transfer path. During the catalytic process, electrons in CB of BOB rapidly recombine with holes in VB of BSO, and the electrons enriched in CB of BSO endow the strong reduction ability for BSOB to trigger efficient photocatalytic nitrogen reduction. As a result, the ammonia yield of BSOB in pure water can reach  $459.04 \mu\text{mol g}^{-1} \text{h}^{-1}$ . This work provides atomic-scale insights for the construction of efficient S-scheme heterojunction photocatalyst based on defect-induced chemical bonding interface.

## Supporting Information

Supporting information is available from the Online Library or from the author.

## CRediT authorship contribution statement

**Yi Zhang:** Conceptualization, Data curation, Investigation, Writing – original draft. **Jun Di:** Data curation, Investigation, Writing – review & editing, Supervision. **Xingwang Zhu:** Data curation, Investigation. **Mengxia Ji:** Resources, Data curation, Investigation. **Chao Chen:** Resources, Supervision. **Yanan Liu:** Data curation, Investigation. **Lina Li:** Data curation, Investigation. **Tiange Wei:** Data curation, Investigation. **Huaming Li:** Resources, Supervision. **Jiexiang Xia:** Conceptualization, Resources, Writing - review & editing, Supervision.

## Declaration of Competing Interest

The authors declare that they have no known competing financial

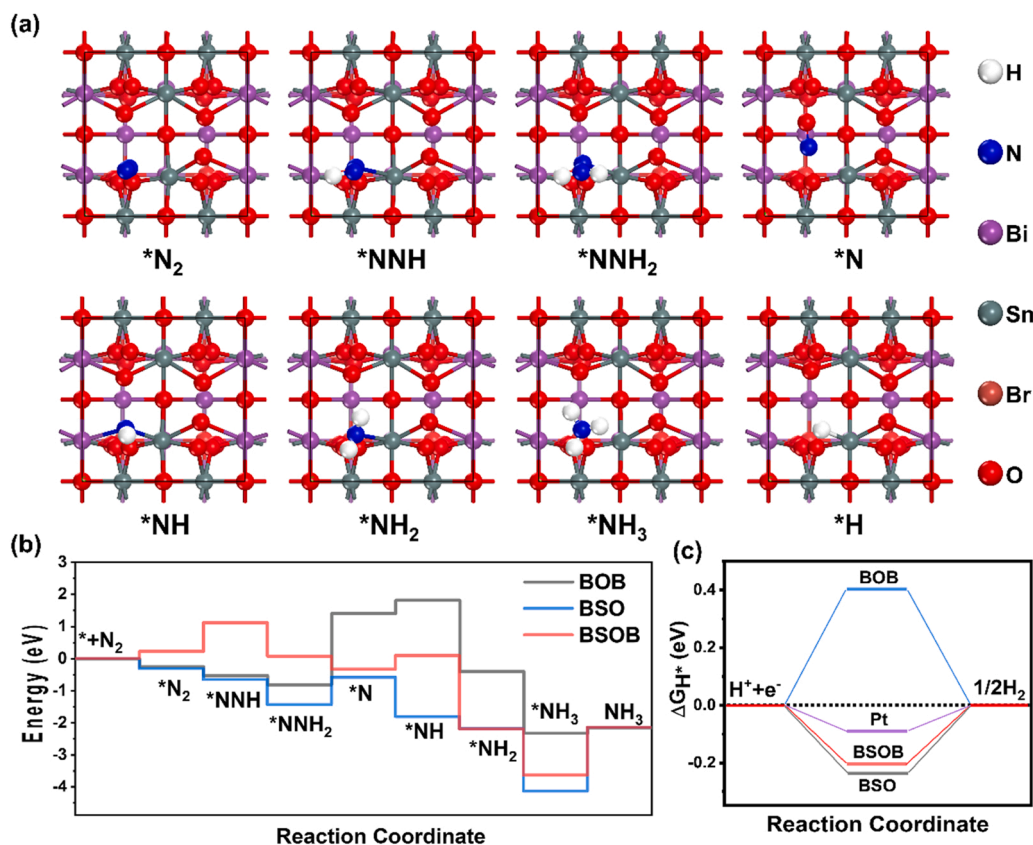


Fig. 5. (a) Schematic diagram of the optimized structure for BSOB; (b) Calculated free-energy diagram for  $N_2$  reduction to  $NH_3$  and (c)  $\Delta G_H^*$  of the samples.

interests or personal relationships that could have appeared to influence the work reported in this paper.

#### Data availability

Data will be made available on request.

#### Acknowledgments

This work was supported by the National Natural Science Foundation of China (No. 21878134 and 22108108).

#### Appendix A. Supporting information

Supplementary data associated with this article can be found in the online version at [doi:10.1016/j.apcatb.2022.122148](https://doi.org/10.1016/j.apcatb.2022.122148).

#### References

- [1] Y. Luo, G.-F. Chen, L. Ding, X. Chen, L.-X. Ding, H. Wang, Efficient electrocatalytic  $N_2$  fixation with mxene under ambient conditions, *Joule* 3 (2019) 279–289, <https://doi.org/10.1016/j.joule.2018.09.011>.
- [2] L.R. Winter, J.G. Chen,  $N_2$  fixation by plasma-activated processes, *Joule* 5 (2021) 300–315, <https://doi.org/10.1016/j.joule.2020.11.009>.
- [3] M.-A. Legare, G. Belanger-Chabot, R.D. Dewhurst, E. Welz, I. Krummenacher, B. Engels, H. Braunschweig, Nitrogen fixation and reduction at boron, *Science* 359 (2018) 896–900, <https://doi.org/10.1126/science.aag1684>.
- [4] M.A.H.J. van Kessel, D.R. Speth, M. Albertsen, P.H. Nielsen, H.J.M. Op den Camp, B. Kartal, M.S.M. Jetten, S. Lucker, Complete nitrification by a single microorganism, *Nature* 528 (2015) 555–559, <https://doi.org/10.1038/nature16459>.
- [5] J. Zhang, Y. Ji, P. Wang, Q. Shao, Y. Li, X. Huang, Adsorbing and activating  $N_2$  on heterogeneous  $Au-Fe_3O_4$  nanoparticles for  $N_2$  fixation, *Adv. Funct. Mater.* 30 (2020), 1906579, <https://doi.org/10.1002/adfm.201906579>.
- [6] Z. Zhao, C. Choi, S. Hong, H. Shen, C. Yan, J. Masa, Y. Jung, J. Qiu, Z. Sun, Surface-engineered oxidized two-dimensional Sb for efficient visible light-driven  $N_2$  fixation, *Nano Energy* 78 (2020), 105368, <https://doi.org/10.1016/j.nanoen.2020.105368>.
- [7] L. Li, C. Tang, D. Yao, Y. Zheng, S.-Z. Qiao, Electrochemical nitrogen reduction: identification and elimination of contamination in electrolyte, *Acs Energy Lett.* 4 (2019) 2111–2116, <https://doi.org/10.1021/acscenergylett.9b01573>.
- [8] J. Zhao, Z. Chen, Single Mo atom supported on defective boron nitride monolayer as an efficient electrocatalyst for nitrogen fixation: a computational study, *J. Am. Chem. Soc.* 139 (2017) 12480–12487, <https://doi.org/10.1021/jacs.7b05213>.
- [9] D.V. Yandulov, R.R. Schrock, Catalytic reduction of dinitrogen to ammonia at a single molybdenum center, *Science* 103 (2003) 17099–17106, <https://doi.org/10.1073/pnas.0602778103>.
- [10] S.-H. Li, M.-Y. Qi, Z.-R. Tang, Y.-J. Xu, Nanostructured metal phosphides: from controllable synthesis to sustainable catalysis, *Chem. Soc. Rev.* 50 (2021) 7539–7586, <https://doi.org/10.1039/D1CS00323B>.
- [11] M.-Y. Qi, M. Conte, M. Anpo, Z.-R. Tang, Y.-J. Xu, Cooperative coupling of oxidative organic synthesis and hydrogen production over semiconductor-based photocatalysts, *Chem. Rev.* 121 (2021) 13051–13085, <https://doi.org/10.1021/acs.chemrev.1c00197>.
- [12] H.-L. Wu, X.-B. Li, C.-H. Tung, L.-Z. Wu, Semiconductor quantum dots: an emerging candidate for  $CO_2$  photoreduction, *Adv. Mater.* 31 (2019), 1900709, <https://doi.org/10.1002/adma.201900709>.
- [13] Y. Yan, J. Gong, J. Chen, Z. Zeng, W. Huang, K. Pu, J. Liu, P. Chen, Recent advances on graphene quantum dots: from chemistry and physics to applications, *Adv. Mater.* 31 (2019), 1808283, <https://doi.org/10.1002/adma.201808283>.
- [14] R.D. Schaller, V.I. Klimov, High efficiency carrier multiplication in PbSe nanocrystals: implications for solar energy conversion, *Phys. Rev. Lett.* 92 (2004), 186601, <https://doi.org/10.1103/PhysRevLett.92.186601>.
- [15] W. Zhou, J.J. Coleman, Semiconductor quantum dots, *Curr. Opin. Solid State Mater. Sci.* 20 (2016) 352–360, <https://doi.org/10.1016/j.cossms.2016.06.006>.
- [16] C. Wang, Y. Li, L. Huang, L. Yang, H. Wang, J. Liu, J. Liu, Z. Song, L. Huang, Enhanced photocatalytic antibacterial and degradation performance by n-p type OD/2D  $SnO_2-x/BiOI$  photocatalyst under LED light, *Chem. Eng. J.* 411 (2021), 128505, <https://doi.org/10.1016/j.cej.2021.128505>.
- [17] M.-Y. Ye, Z.-H. Zhao, Z.-F. Hu, L.-Q. Liu, H.-M. Ji, Z.-R. Shen, T.-Y. Ma, OD/2D heterojunctions of vanadate quantum dots/graphitic carbon nitride nanosheets for enhanced visible-light-driven photocatalysis, *Angew. Chem. Int. Ed.* 56 (2017) 8407–8411, <https://doi.org/10.1002/anie.201611127>.
- [18] P. Ma, X. Zhang, C. Wang, Z. Wang, K. Wang, Y. Feng, J. Wang, Y. Zhai, J. Deng, L. Wang, K. Zheng, Band alignment of homojunction by anchoring CN quantum dots on g- $C_3N_4$  (OD/2D) enhance photocatalytic hydrogen peroxide evolution, *Appl. Catal. B* 300 (2022), 120736, <https://doi.org/10.1016/j.apcatb.2021.120736>.



- [19] Y. Chao, P. Zhou, N. Li, J. Lai, Y. Yang, Y. Zhang, Y. Tang, W. Yang, Y. Du, D. Su, Y. Tan, S. Guo, Ultrathin visible-light-driven Mo incorporating  $\text{In}_2\text{O}_3\text{-ZnIn}_2\text{Se}_4$  Z-Scheme Nanosheet Photocatalysts, *Adv. Mater.* 31 (2019), 1807226, <https://doi.org/10.1002/adma.201807226>.
- [20] F. Xu, K. Meng, B. Cheng, S. Wang, J. Xu, J. Yu, Unique S-scheme heterojunctions in self-assembled  $\text{TiO}_2/\text{CsPbBr}_3$  hybrids for  $\text{CO}_2$  photoreduction, *Nat. Commun.* 11 (2020) 4613, <https://doi.org/10.1038/s41467-020-18350-7>.
- [21] J. Di, B. Lin, B. Tang, S. Guo, J. Zhou, Z. Liu, Engineering cocatalysts onto low-dimensional photocatalysts for  $\text{CO}_2$  reduction, *Small Struct.* 2 (2021), 2100046, <https://doi.org/10.1002/ssstr.202100046>.
- [22] S. Li, L. Zhang, W. Zhao, S. Yuan, L. Yang, X. Chen, P. Ge, W. Sun, X. Ji, Designing interfacial chemical bonds towards advanced metal-based energy-storage/conversion materials, *Energy Stor. Mater.* 32 (2020) 477–496, <https://doi.org/10.1016/j.ensm.2020.07.023>.
- [23] X. Chen, J.-Y. Li, Z.-R. Tang, Y.-J. Xu, Surface-defect-engineered photocatalyst for nitrogen fixation into value-added chemical feedstocks, *Catal. Sci. Technol.* 10 (2020) 6098–6110, <https://doi.org/10.1039/D0CY01227K>.
- [24] S. Li, L. Meng, W. Tian, L. Li, Engineering interfacial band bending over  $\text{ZnIn}_2\text{S}_4/\text{SnS}_2$  by interface chemical bond for efficient solar-driven photoelectrochemical water splitting, *Adv. Energy Mater.* (2022), 2200629, <https://doi.org/10.1002/aenm.202200629>.
- [25] J. Di, C. Chen, C. Zhu, P. Song, J. Xiong, M. Ji, J. Zhou, Q. Fu, M. Xu, W. Hao, J. Xia, S. Li, H. Li, Z. Liu, Bismuth vacancy-tuned bismuth oxybromide ultrathin nanosheets toward photocatalytic  $\text{CO}_2$  reduction, *ACS Appl. Mater. Interfaces* 11 (2019) 30786–30792, <https://doi.org/10.1021/acsami.9b08109>.
- [26] J. Di, C. Chen, C. Zhu, R. Long, H.L. Chen, X.Z. Cao, J. Xiong, Y.X. Weng, L. Song, S. Z. Li, H.M. Li, Y.J. Xiong, Z. Liu, Surface local polarization induced by bismuth-oxygen vacancy pairs tuning non-covalent interaction for  $\text{CO}_2$  photoreduction, *Adv. Energy Mater.* 11 (2021), 2102389, <https://doi.org/10.1002/aenm.202102389>.
- [27] A. Salamat, A.L. Hector, P.F. McMillan, C. Ritter, Structure, bonding, and phase relations in  $\text{Bi}_2\text{Sn}_2\text{O}_7$  and  $\text{Bi}_2\text{Ti}_2\text{O}_7$  pyrochlores: new insights from high pressure and high temperature studies, *Inorg. Chem.* 50 (2011) 11905–11913, <https://doi.org/10.1021/ic200841v>.
- [28] D. Zhao, Y. Wang, C.-L. Dong, Y.-C. Huang, J. Chen, F. Xue, S. Shen, L. Guo, Boron-doped nitrogen-deficient carbon nitride-based Z-scheme heterostructures for photocatalytic overall water splitting, *Nat. Energy* 6 (2021) 388–397, <https://doi.org/10.1038/s41560-021-00795-9>.
- [29] R.X. Silva, C.W.A. Paschoal, R.M. Almeida, M. Carvalho Castro Jr., A.P. Ayala, J. T. Auletta, M.W. Lufaso, Temperature-dependent Raman spectra of  $\text{Bi}_2\text{Sn}_2\text{O}_7$  ceramics, *Vib. Spectrosc.* 64 (2013) 172–177, <https://doi.org/10.1016/j.vibspec.2012.05.009>.
- [30] X. Xue, R. Chen, H. Chen, Y. Hu, Q. Ding, Z. Liu, L. Ma, G. Zhu, W. Zhang, Q. Yu, J. Liu, J. Ma, Z. Jin, Oxygen vacancy engineering promoted photocatalytic ammonia synthesis on ultrathin two-dimensional bismuth oxybromide nanosheets, *Nano Lett.* 18 (2018) 7372–7377, <https://doi.org/10.1021/acs.nanolett.8b03655>.
- [31] Y.-D. Xu, C. Wang, Y.-Y. Lv, Y.B. Chen, S.-H. Yao, J. Zhou, Infrared and Raman spectra of  $\text{Bi}_2\text{O}_2\text{X}$  and  $\text{Bi}_2\text{O}_2\text{X}_2$  (X = S, Se, and Te) studied from first principles calculations, *RSC Adv.* 9 (2019) 18042–18049, <https://doi.org/10.1039/C9RA02584G>.
- [32] X.-D. Wang, Y.-H. Huang, J.-F. Liao, Y. Jiang, L. Zhou, X.-Y. Zhang, H.-Y. Chen, D.-B. Kuang, In situ construction of a  $\text{Cs}(2)\text{Sn}(6)$  perovskite nanocrystal/ $\text{SnS}_2$  nanosheet heterojunction with boosted interfacial charge transfer, *J. Am. Chem. Soc.* 141 (2019) 13434–13441, <https://doi.org/10.1021/jacs.9b04482>.
- [33] Y.-J. Yuan, Z.-K. Shen, S. Song, J. Guan, L. Bao, L. Pei, Y. Su, S. Wu, W. Bai, Z.-T. Yu, Z. Ji, Z. Zou, Co-P bonds as atomic-level charge transfer channel to boost photocatalytic  $\text{H}_2$  production of  $\text{Co}_2\text{P}$ /black phosphorus nanosheets photocatalyst, *ACS Catal.* 9 (2019) 7801–7807, <https://doi.org/10.1021/acscatal.9b02274>.
- [34] S.L. Yang, X.X. Deng, P. Chen, T.X. Zhao, F. Liu, C.Y. Deng, S.-F. Yin, Linker functionalized poly(heptazine imide) as charge channel and activation site for enhancing photocatalytic nitrogen fixation in pure water, *Appl. Catal. B* 311 (2022), 121370, <https://doi.org/10.1016/j.apcatb.2022.121370>.
- [35] G.A. Wang, T.T. Huo, Q.H. Deng, F. Yu, Y.G. Xia, H.P. Li, W.G. Hou, Surface-layer bromine doping enhanced generation of surface oxygen vacancies in bismuth molybdate for efficient photocatalytic nitrogen fixation, *Appl. Catal. B* 310 (2022), 121319, <https://doi.org/10.1016/j.apcatb.2022.121319>.
- [36] X.A. Dong, Z.H. Cui, X. Shi, P. Yan, Z.M. Wang, A.C. Co, F. Dong, Insights into dynamic surface bromide sites in  $\text{Bi}_4\text{O}_5\text{Br}_2$  for sustainable  $\text{N}_2$  photofixation, *Angew. Chem. Int. Ed.* (2022), e202200937, <https://doi.org/10.1002/anie.202200937>.
- [37] B.B. Guo, X.Y. Cheng, Y. Tang, W. Guo, S.Q. Deng, L. Wu, X.Z. Fu, Dehydrated  $\text{UiO-66}(\text{SH})_2$ : The Zr-O cluster and its photocatalytic role mimicking the biological nitrogen fixation, *Angew. Chem. Int. Ed.* 61 (2022), e202117244, <https://doi.org/10.1002/anie.202117244>.
- [38] Y.T. Zhang, L. Ran, Y.X. Zhang, P.L. Zhai, Y.Z. Wu, J.F. Gao, Z.W. Li, B. Zhang, C. Wang, Z.Z. Fan, X.M. Zhang, J.Q. Cao, D.F. Jin, L.C. Sun, J.G. Hou, Two-dimensional defective boron-doped niobic acid nanosheets for robust nitrogen photofixation, *ACS Nano* 15 (2021) 17820–17830, <https://doi.org/10.1021/acsnano.1c06017>.
- [39] Q.T. Han, X.W. Bai, J.M. Chen, S.N. Feng, W. Gao, W.G. Tu, X.Y. Wang, J.L. Wang, B. Jia, Q. Shen, Y. Zhou, Z.G. Zou, Hollow  $\text{InVO}_4$  nanocuboid assemblies toward promoting photocatalytic  $\text{N}_2$  conversion performance, *Adv. Mater.* 33 (2021), 2006780, <https://doi.org/10.1002/adma.202006780>.
- [40] L.W. Chen, Y.C. Hao, Y. Guo, Q.H. Zhang, J. Li, W.Y. Gao, L.T. Ren, X. Su, L.Y. Hu, N. Zhang, S.W. Li, X. Feng, L. Gu, Y.W. Zhang, A.X. Yin, B. Wang, Metal-organic membranes encapsulating gold nanoparticles for direct plasmonic photocatalytic nitrogen fixation, *J. Am. Chem. Soc.* 143 (2021) 5727–5736, <https://doi.org/10.1021/jacs.0c13342>.
- [41] Y.D. Zhang, T.T. Hou, Q. Xu, Q.Y. Wang, Y. Bai, S.K. Yang, D.W. Rao, L.H. Wu, H. B. Pan, J.F. Chen, G.M. Wang, J.F. Zhu, T. Yao, X.S. Zheng, Dual-metal sites boosting polarization of nitrogen molecules for efficient nitrogen photofixation, *Adv. Sci.* 8 (2021), 2100302, <https://doi.org/10.1002/adv.202100302>.
- [42] Y.N. Bo, H.Y. Wang, Y.X. Lin, T. Yang, R. Ye, Y. Li, C.Y. Hu, P.Y. Du, Y.G. Hu, Z. Liu, R. Long, C. Gao, B.J. Ye, L. Song, X.J. Wu, Y.J. Xiong, Altering hydrogenation pathways in photocatalytic nitrogen fixation by tuning local electronic structure of oxygen vacancy with dopant, *Angew. Chem. Int. Ed.* 60 (2021) 16085–16092, <https://doi.org/10.1002/anie.202104001>.
- [43] K.Q. Hu, P.X. Qiu, L.W. Zeng, S.X. Hu, L. Mei, S.W. An, Z.W. Huang, X.H. Kong, J. H. Lan, J.P. Yu, Z.H. Zhang, Z.F. Xu, J.K. Gibson, Z.F. Chai, Y.F. Bu, W.Q. Shi, Solar-driven nitrogen fixation catalyzed by stable radical-containing MOFs: improved efficiency induced by a structural transformation, *Angew. Chem. Int. Ed.* 59 (2020) 20666–20671, <https://doi.org/10.1002/anie.202009630>.
- [44] Y.X. Zhao, L.R. Zheng, R. Shi, S. Zhang, X.A. Bian, F. Wu, X.Z. Cao, G.I. N. Waterhouse, T. Zhang, Alkali etching of layered double hydroxide nanosheets for enhanced photocatalytic  $\text{N}_2$  reduction to  $\text{NH}_3$ , *Adv. Energy Mater.* 10 (2020), 2002199, <https://doi.org/10.1002/aenm.202002199>.
- [45] X. Ruan, X. Cui, Y. Cui, X. Fan, Z. Li, T. Xie, K. Ba, G. Jia, H. Zhang, L. Zhang, W. Zhang, X. Zhao, J. Leng, S. Jin, D.J. Singh, W. Zheng, Favorable energy band alignment of  $\text{TiO}_2$  anatase/rutile heterophase homojunctions yields photocatalytic hydrogen evolution with quantum efficiency exceeding 45.6%, *Adv. Energy Mater.* 12 (2022), 2200298, <https://doi.org/10.1002/aenm.202200298>.
- [46] X. Chen, M.-Y. Qi, Y.-H. Li, Z.-R. Tang, Y.-J. Xu, Enhanced ambient ammonia photosynthesis by Mo-doped  $\text{Bi}_5\text{O}_7\text{Br}$  nanosheets with light-switchable oxygen vacancies, *Chin. J. Catal.* 42 (2021) 2020–2026, [https://doi.org/10.1016/S1872-2067\(21\)63837-8](https://doi.org/10.1016/S1872-2067(21)63837-8).
- [47] L. Lin, C. Hou, X. Zhang, Y. Wang, Y. Chen, T. He, Highly efficient visible-light driven photocatalytic reduction of  $\text{CO}_2$  over  $\text{g-C}_3\text{N}_4$  nanosheets/tetra(4-carboxyphenyl) porphyrin iron (III) chloride heterogeneous catalysts, *Appl. Catal. B* 221 (2018) 312–319, <https://doi.org/10.1016/j.apcatb.2017.09.033>.
- [48] X. Chen, X. Zhang, Y.-H. Li, M.-Y. Qi, J.-Y. Li, Z.-R. Tang, Z. Zhou, Y.-J. Xu, Transition metal doping  $\text{BiOBr}$  nanosheets with oxygen vacancy and exposed {102} facets for visible light nitrogen fixation, *Appl. Catal. B* 281 (2021), 119516, <https://doi.org/10.1016/j.apcatb.2020.119516>.
- [49] K. Ding, A.W. Pierpont, W.W. Brennessel, G. Lukat-Rodgers, K.R. Rodgers, T. R. Cundari, E. Bill, P.L. Holland, Cobalt-dinitrogen complexes with weakened N-N bonds, *J. Am. Chem. Soc.* 131 (2009) 9471–9474, <https://doi.org/10.1021/ja808783u>.
- [50] Y. Zhang, J. Di, X. Qian, M. Ji, Z. Tian, L. Ye, J. Zhao, S. Yin, H. Li, J. Xia, Oxygen vacancies in  $\text{Bi}_2\text{Sn}_2\text{O}_7$  quantum dots to trigger efficient photocatalytic nitrogen reduction, *Appl. Catal. B* 299 (2021), 120680, <https://doi.org/10.1016/j.apcatb.2021.120680>.
- [51] X. Dong, Z. Cui, X. Shi, P. Yan, Z. Wang, A.C. Co, F. Dong, Insights into dynamic surface bromide sites in  $\text{Bi}_4\text{O}_5\text{Br}_2$  for sustainable  $\text{N}_2$  photofixation, *Angew. Chem. Int. Ed.* 61 (2022), e202200937, <https://doi.org/10.1002/anie.202200937>.
- [52] Q. Zhou, Q. Hao, Y. Li, J. Yu, C. Xu, H. Liu, S. Yan, Free-standing trimodal porous NiZn intermetallic and Ni heterojunction as highly efficient hydrogen evolution electrocatalyst in the alkaline electrolyte, *Nano Energy* 89 (2021), 106402, <https://doi.org/10.1016/j.nanoen.2021.106402>.